Mixture segregation within sonoluminescence bubbles

By BRIAN D. STOREY AND ANDREW J. SZERI

Department of Mechanical Engineering, University of California, Berkeley,
CA 94720-1740, USA

This paper concerns a relaxation of the assumption of uniform mixture composition in the interior of sonoluminescence bubbles. Intense temperature and pressure gradients within the bubble drive relative mass diffusion which overwhelms diffusion driven by concentration gradients. This thermal and pressure diffusion results in a robust compositional inhomogeneity in the bubble which lasts several orders of magnitude longer than the temperature peak or light pulse at the main collapse of the bubble. This effect has important consequences for control of sonoluminescence, gas dynamics, sonochemistry, and the physics of light production.

1. Introduction

It is common for sonoluminescence (SL) experiments to be performed with air and other gas or gas–vapour mixtures. Current SL models assume, if two gases are present, that the components remain uniformly distributed throughout the bubble. However, with the extremely large temperature and pressure gradients in the interior of the bubble, one should be very careful in ruling out the possibility of species segregation. While the phenomena of diffusive mass flux due to temperature and pressure gradients are well known (Bird, Stewart & Lightfoot 1960), they are often neglected due to their small consequence in many applications. The temperature and pressure gradients that exist in SL can be quite large and the possibility of species segregation should be addressed.

Thermal diffusion is the tendency for a mixture of gases to segregate due to a large temperature gradient. This phenomenon was first a theoretical conjecture of the Chapman–Enskog theory and later confirmed through experimentation (Chapman & Cowling 1990). In a noble gas mixture molecules of the species with the larger molecular mass will be driven to the cooler regions. In SL, thermal diffusion might be expected to play a role during the collapse of the bubble when the centre is extremely hot and the bubble wall is relatively cool. The temperature gradient in the bubble is a consequence of the compression heating of the bubble contents and the heat flux out to the surrounding liquid (Vuong & Szeri 1996). If the mixture is composed of noble gases, this temperature gradient will drive lighter species toward the centre.

Pressure diffusion is the principle on which the centrifuge operates, where lighter molecules in a mixture tend to the low-pressure regions. In SL, the accelerating bubble wall creates a compression wave during the main collapse. As this wave builds, it will tend to push the light molecules in the mixture to the centre faster than the heavy molecules. When the compression wave reflects at the origin, pressure diffusion will tend to push the lighter molecules away from the centre and towards the bubble wall.

From these arguments it seems that thermal and pressure diffusion will tend to drive the lighter molecules to the centre prior to the moment of minimum radius. It remains to be determined what will happen when the compression wave reflects at the centre because the thermal and pressure diffusion will oppose one another. While the driving forces behind species segregation clearly exist, it is unclear whether the species will have time to separate during the rapid bubble collapse. Moreover, conventional diffusion (driven by concentration gradients) will tend to oppose any compositional inhomogeneities that may arise by thermal and pressure diffusion. In this paper, we present a computational study of a bubble composed of a mixture of two noble gases. We investigate whether or not species tend to segregate under typical conditions of single and multi-bubble sonoluminescence.

There may be many consequences of species segregation. First there is the issue of correct numerical simulation of SL bubbles composed of gas mixtures. A number of computational studies of air bubbles, for example, have neglected the possible segregation of air into components within the bubble interior. We note that bubbles are always composed of mixtures because vapour from the liquid will be present.

From the point of view of gas dynamics, species segregation may play an important role in the formation of shock waves within SL bubbles. If species segregation occurs, then the mean molecular weight of the mixture will change within the bubble. The sound speed, which is dependent on molecular weight, will be variable in space due to compositional inhomogeneities (as well as temperature and pressure variations). Gradients in sound speed have a large influence on whether compression waves are able to steepen into shocks (Vuong, Szeri & Young 1999).

Species segregation also affects chemical reactions inside SL bubbles. In single-bubble SL the argon rectification hypothesis of Lohse and collaborators (Lohse *et al.* 1997) has gained considerable acceptance. The hypothesis is that diatomic species in air undergo dissociation and re-combine into highly soluble products that subsequently dissolve into the liquid, leaving the inert argon behind. Species segregation should be accounted for when considering: (i) whether the reactants are at the centre when the bubble is hot, and (ii) whether the products of reaction are able to move to the bubble wall where they can be absorbed.

A similar consequence of species segregation is related to cavitation thermometry (Bernstein *et al.* 1996). In cavitation thermometry, well understood spectral emissions from volatile contaminants are used to study temperatures within cavitation bubbles. Knowledge of where the volatile species go in the gas phase will help in interpreting such measurements. Similar questions will be of interest in sonochemistry applications.

Finally, a knowledge of compositional inhomogeneities may be essential in understanding the light emission process in single-bubble SL. All of these points may lead to better control of the phenomenon.

2. Formulation

We assume that the bubble is spherical and is composed of a mixture of two monatomic gases. For the present model we assume that liquid vapour is not present in the bubble. We make this assumption to avoid the complications caused by evaporation and condensation at the bubble interface, but shall relax it in future work. We assume that no mass transport occurs across the bubble interface. Furthermore, we neglect heat transfer by radiation and make no attempt to model the light emission. We emphasize that the Navier–Stokes equations remain valid throughout the bubble collapse because the relative gradients (in temperature, pressure, velocity,

and concentration) always have length scales much longer than the mean free path of the molecules (Hirschfelder, Curtiss & Bird 1954).

2.1. *Gas dynamics*

The conservation of mass for a two-species mixture in spherical Eulerian coordinates is expressed as (Bird *et al.* 1960)

$$\frac{D\rho}{Dt} = -\rho \frac{1}{r^2} \frac{\partial r^2 v}{\partial r}, \tag{2.1}$$

$$\frac{D\rho_A}{Dt} = -\rho_A \frac{1}{r^2} \frac{\partial r^2 v}{\partial r} - \frac{1}{r^2} \frac{\partial r^2 j_A}{\partial r}. \tag{2.2}$$

Here D/Dt is the material derivative, ρ is the density, ρ_A is the mass concentration of species A, r is the radial coordinate, and v is the mass average radial velocity. The diffusive mass flux of species $A(B)$ relative to the mass average velocity (assuming an ideal mixture), $j_{A(B)}$, is

$$j_A = -j_B = -\left(\frac{\rho}{M^2}\right) M_A M_B D_{AB} \left[\frac{\partial x_A}{\partial r} + \frac{M}{\rho \bar{R} T}(x_A - w_A)\frac{\partial P}{\partial r} + k_T \frac{\partial lnT}{\partial r}\right], \tag{2.3}$$

where M is the number-mean molecular weight, $M_{A(B)}$ is the molecular weight of species $A(B)$, w_A is the mass fraction of species A, x_A is the mole fraction of species A, P is the pressure, T is the temperature, k_T is the thermal diffusion ratio, $D_{AB}(T, P, x_A)$ is the binary diffusion coefficient, and $\bar{R}$ is the universal gas constant. The balance of linear momentum in the radial direction is

$$\rho \frac{Dv}{Dt} = -\frac{\partial P}{\partial r} - \frac{1}{r^2}\frac{\partial r^2 \tau_{rr}}{\partial r} + \frac{\tau_{\theta\theta} + \tau_{\phi\phi}}{r}, \tag{2.4}$$

where the components of the stress in the radial and angular directions are

$$\tau_{rr} = -2\tau_{\theta\theta} = -2\tau_{\phi\phi} = \frac{-4\mu(T, P, x_A)}{3}\left(\frac{\partial v}{\partial r} - \frac{v}{r}\right),$$

and the viscosity, μ, is variable with temperature, pressure, and composition. The balance of energy is

$$\rho \frac{DE}{Dt} = -\frac{1}{r^2}\frac{\partial}{\partial r}[r^2(q + \tau_{rr}v + Pv)], \tag{2.5}$$

where E, the total energy, is the internal energy plus the kinetic energy, and the heat flux in the radial direction, q, is

$$q = -k(T, P, x_A)\frac{\partial T}{\partial r} + (h_A - h_B)j_A,$$

where k is the variable thermal conductivity and $h_{A(B)}$ is the enthalpy of species $A(B)$ at the local temperature and pressure. We neglect the Dufour energy flux and the radiant energy flux in the energy equation. The Dufour term is a temperature gradient caused by the mass flux. A scaling analysis shows this term to be much smaller than the other terms in the energy balance and it is therefore neglected. A full numerical calculation including this term confirms it is of minimal consequence.

Following Vuong & Szeri (1996), we cast the equations into Lagrangian form, where $r(a, t)$ is the radial coordinate at time t of the marker particle that was at radial position a at $t = 0$. The Lagrangian form is convenient because it eliminates

the need to track the moving bubble interface in the computational domain. In this formulation, the Lagrangian marker particles move with the mass average velocity, but the composition of the marker particles is not fixed. Hence, the material derivative $\mathrm{D}/\mathrm{D}t \equiv \partial/\partial t + v\partial/\partial r$ of a field regarded as a function of radius r and time t becomes simply $\partial/\partial t$ computed holding a (the Lagrangian radial coordinate) constant.

We make the equations dimensionless using the initial values of radius R_0, density ρ_0, pressure P_0, and temperature T_0. The velocity scale, v_0, is $(P_0/\rho_0)^{1/2}$, the mass flux scale is $\rho_0 v_0$, and the energy and enthalpy are scaled by v_0^2. We make the transport coefficients (μ, k, and D_{AB}) dimensionless by dividing by the values at the initial state. Using a hat to denote dimensionless Lagrangian variables, the mass conservation equations become

$$\hat{\rho}J = 1, \tag{2.6}$$

$$\frac{\partial \hat{w}_A}{\partial \hat{t}} = -\frac{1}{\hat{a}^2}\frac{\partial(\hat{r}^2\hat{j}_A)}{\partial \hat{a}}, \tag{2.7}$$

where the Jacobian of the transformation between the the current and reference configurations, J, is given by

$$J = \frac{r^2}{a^2}\frac{\partial r}{\partial a},$$

and the radial diffusive mass flux, $\hat{j}_A$, is

$$\hat{j}_A = -\frac{M_A M_B}{M_0^2}\frac{1}{ReSc}\frac{\hat{D}_{AB}}{\hat{M}^2\hat{J}}\frac{\partial \hat{a}}{\partial \hat{r}}\left[\frac{\partial \hat{x}_A}{\partial \hat{a}} + \frac{\hat{M}\hat{J}}{\hat{T}}Z_0(\hat{x}_A - \hat{w}_A)\frac{\partial \hat{P}}{\partial \hat{a}} + k_T\frac{\partial ln\hat{T}}{\partial \hat{a}}\right].$$

Here, Z_0 is the compressibility in the initial state (equal to 1 for an ideal gas). The Schmidt number, $Sc \equiv \mu_0/\rho_0 D_{AB}$, is the ratio of the diffusivity of momentum to the diffusivity of mass and the Reynolds number is $Re \equiv \rho_0 R_0 v_0/\mu_0$. The balance of linear momentum becomes

$$\frac{\partial \hat{v}}{\partial \hat{t}} = -\frac{\hat{r}^2}{\hat{a}^2}\frac{\partial \hat{P}}{\partial \hat{a}} - \hat{\tau}\frac{3\hat{r}}{\hat{a}^2}\frac{\partial \hat{r}}{\partial \hat{a}} - \frac{\hat{r}^2}{\hat{a}^2}\frac{\partial \hat{\tau}}{\partial \hat{a}}, \tag{2.8}$$

where the stress is

$$\hat{\tau} = \frac{-4\hat{\mu}}{3Re}\left(\frac{\partial \hat{v}}{\partial \hat{a}}\frac{\partial \hat{a}}{\partial \hat{r}} - \frac{\hat{v}}{\hat{r}}\right).$$

The energy equation in these variables becomes

$$\frac{\partial \hat{E}}{\partial \hat{t}} = -\frac{1}{\hat{a}^2}\frac{\partial}{\partial \hat{a}}[\hat{r}^2(\hat{q} + \hat{\tau}\hat{v} + \hat{P}\hat{v})], \tag{2.9}$$

where the radial heat flux is

$$\hat{q} = -\frac{C_{p0}T_0\rho_0}{P_0}\frac{\hat{k}}{RePr}\frac{\partial \hat{T}}{\partial \hat{a}}\frac{\partial \hat{a}}{\partial \hat{r}} + (\hat{h}_A - \hat{h}_B)\hat{j}_A,$$

with C_{p0} the specific heat and Prandtl number $Pr \equiv C_{p0}\mu_0/k_0$. We note $C_{p0}T_0\rho_0/P_0 = \gamma/(\gamma - 1)$ for a perfect gas where γ is the ratio of specific heats.

2.2. *Equation of state and transport properties*

An equation of state (EOS) is required to close the gas dynamics problem. Due to the extreme temperatures and pressures in SL, we avoid the shortcomings of less sophisticated equations of state and use a van der Waals type model (Vuong *et al.* 1999). This EOS divides the internal energy into the sum of a cold ($T = 0\,\mathrm{K}$) energy,

a nuclear motion energy, and an electron energy where each of the different energies were fit to experimental data. The partial pressure is similarly divided. This EOS is accurate over a very large range of densities and temperatures. It should be noted that using a standard van der Waals EOS (and assuming constant specific heats) gives qualitatively the same results as the more complex EOS.

Because we consider a mixture of gases, we also need equations for mixture thermodynamics. We take a straightforward approach and simply add the partial pressures and energies of the individual gas components. These mixture relations are built into the governing equations in the evaluation of the partial molal properties.

The transport properties are functions of concentration, temperature, and pressure. In order to account for these variations we use the Chapman–Enskog theory with a Lennard–Jones 12-6 potential and corrections for dense gases and high temperatures. The details of the equations are given in the Appendix.

We compared results from the Chapman–Enskog equations with our corrections to some available data at both high temperature and high density and found the equations to be reasonably accurate (Sengers 1965; Amdur & Mason 1954; Hirschfelder *et al.* 1954). Vuong & Szeri (1996) showed that the exact functional form of the transport properties did not play a major role in the results of SL computations. We feel the Chapman–Enskog equations provide reasonable results as the equations predict the proper trends in transport properties with changes in temperature, pressure, and composition. We also feel this is a better approach than previous attempts where the transport properties were taken to be a function of temperature only. It should be noted that the Chapman–Enskog theory must be adjusted if the gas ionizes. Ionization changes the nature of the molecular potential and can drastically affect the transport properties including a change in the sign of the thermal diffusion ratio (Chapman & Cowling 1990). Included in the EOS is a computation of the degree of ionization. We use this computation to check that our transport properties are valid.

2.3. *Motion of the liquid*

The coupling of the Navier–Stokes equations in the liquid and the gas governs the response of the bubble to the applied acoustic field. However, due to the spherical symmetry of the problem, the partial differential equations that govern the liquid motion can be reduced to a single ordinary differential equation for the bubble radius. This equation has various forms and the derivations, assumptions, and limitations of these forms can be found in many references. The form we use, often referred to as the Gilmore equation (Prosperetti & Lezzi 1986), accounts for compressibility of the liquid and is

$$(1 - M)R\ddot{R} + \tfrac{3}{2}(1 - \tfrac{1}{3}M)\dot{R}^2 = (1 + M)H + \frac{R}{c_{l,b}}(1 - M)\dot{H}. \qquad (2.10)$$

Here R is the time-dependent bubble radius, dots denote a time derivative, H is the liquid enthalpy, $c_{l,b}$ is the speed of sound in the liquid at the bubble wall, and M is the bubble wall Mach number $\dot{R}/c_{l,b}$. This equation is non-dimensionalized with the same variables as the gas dynamics problem. We use the modified Tait form of the equation of state for the liquid water, which gives the following relationships:

$$\frac{P_l + B}{P_{l,o} + B} = \left(\frac{\rho_l}{\rho_{l,o}}\right)^n,$$

$$c_l^2 = \frac{n(P_l + B)}{\rho_l}.$$

Here, P_l is the pressure in the liquid and ρ_l is the liquid density. The constants $n = 7.15$ and $B = 3049.13$ bar are valid to 10^5 bar. This equation of state gives the enthalpy in the liquid as

$$H_{l,b} = \frac{n}{n-1} \left(\frac{P_{l,b} + B}{\rho_{l,b}} - \frac{P_{l,\infty} + B}{\rho_{l,\infty}} \right),$$

$$P_{l,b} = P_g - \tau_{rr} - \frac{4\dot{R}}{Re_l R} - \frac{\sigma(T)}{WeR},$$

$$P_{l,\infty} = (1 - P_a \sin \omega t) \frac{P_{L,o}}{P_o}.$$

The subscript l,b refers to properties in the liquid at the bubble wall, subscript l,∞ refers to properties infinitely far from the bubble, P_g is the gas pressure at the bubble wall from the gas dynamics problem, Re_l is the Reynolds number based on the liquid viscosity, $We \equiv R_o P_o / 2\sigma_o$ is the Weber number, σ is the (temperature-dependent) surface tension, P_a is the sound pressure amplitude ratio, and ω is the sound frequency.

The surface tension is taken to be a function of temperature. In many previous works, the surface tension was assumed to be a constant or neglected altogether. Assuming a constant value is not quite correct. Upon collapse, the temperature of the bubble wall can exceed the critical point very briefly, a condition where there is no longer a clearly defined liquid–gas interface and the surface tension is zero. To neglect surface tension is also inaccurate as the surface tension tends to smooth the bubble collapse before the wall temperature gets much above the initial temperature (Yuan *et al.* 1998). As a better approximation we use a surface tension that is variable with temperature and goes to zero at the critical point. The empirical equation for liquid water that we use is (Carey 1992)

$$\sigma = 235.8 \left(1 - \frac{T}{T_c} \right)^{1.256} \left[1 - 0.625 \left(1 - \frac{T}{T_c} \right) \right],$$

where T is the temperature of the interface, T_c is the critical temperature, and σ is in units of $\mathrm{mN\,m^{-1}}$.

2.4. *Temperature of the bubble interface*

Heat transfer between the bubble and the surrounding liquid is of major importance to the gas dynamics at the collapse (Vuong & Szeri 1996; Vuong *et al.* 1999). In order to account for heat transfer leaving the bubble, one must solve the energy equation in the liquid and match the temperature and heat flux at the gas–liquid boundary. The energy balance in the liquid in dimensional, Eulerian variables is

$$\frac{\mathrm{D}T}{\mathrm{D}t} = \frac{k_l}{\rho_l C_{pl}} \frac{1}{r^2} \frac{\partial}{\partial r} \left(r^2 \frac{\partial T}{\partial r} \right), \tag{2.11}$$

where ρ_l, k_l, and C_{pl} are the density, thermal conductivity, and specific heat of the liquid. We assume that the thermo-physical properties do not vary with temperature. Following Eller & Flynn (1965) and Fyrillas & Szeri (1994) we transform the space coordinate to a dimensionless Lagrangian boundary layer coordinate, $s \equiv \sqrt{Pe}(r^3 - R^3)/(3R_0^3)$, and time into a nonlinear time $\tau \equiv \int_0^t R(t)^4 \, \mathrm{d}t$. The Péclet number, $Pe \equiv Re_l Pr_l$, is based on the liquid properties. In terms of the temperature difference,

$\theta \equiv T - T_\infty$, the energy equation is simplified to the linear heat conduction equation

$$\frac{\partial \theta}{\partial \tau} = \frac{\partial^2 \theta}{\partial s^2}. \tag{2.12}$$

Because the interface cannot store thermal energy, the dimensionless heat flux out of the bubble, $\hat{g}(\tau)$, satisfies

$$\hat{g}(\tau) = \frac{\partial \theta}{\partial s} = \frac{k_0 \hat{k}(T, P, x_A)}{k_l} \frac{1}{\sqrt{Pe}\hat{R}^2} \frac{\partial \hat{T}}{\partial \hat{r}} \bigg|_{\hat{r}=\hat{R}}. \tag{2.13}$$

We regard the heat flux as known from the gas dynamics, and append two additional conditions $\theta(\tau, \infty) = 0$ and $\theta(0, s) = 0$.

2.5. *Numerical method*

We solve the governing partial differential equations in the gas with a spectral collocation (or pseudospectral) method. The details of collocation methods can be found in many references such as Canuto *et al.* (1988) and Boyd (1989). We approximate the fields of interest (i.e. $r(a, t), v(a, t), T(a, t) \ldots$) by projecting them into an N-dimensional function sub-space spanned by Chebyshev polynomial basis functions. Explicitly, this approximation is

$$X(a, t) \approx \sum_{n=0}^{N} b_n(t) T_n(a), \tag{2.14}$$

where $X(a, t)$ is a field that is a function of radius (in the reference configuration) and time, $b_n(t)$ are the time-dependent Chebyshev coefficients, and $T_n(a)$ are the Chebyshev polynomials. Spectral collocation methods satisfy the governing equations exactly at certain radial locations, the collocation points, which we selected to be

$$a_k = \cos \frac{\pi(k - N)}{2N + 1}, \ k = 0, 1, \ldots, N.$$

The Chebyshev polynomials serve as the interpolating functions between these points.

To satisfy exactly the conditions at the centre related to the assumption of spherical symmetry, we expand the spatial quantities (i.e. temperature, pressure, mole fraction, etc.) in the even polynomials T_{2n}, and vector quantities (i.e. velocity and fluxes) in odd polynomials T_{2n+1}. The boundary conditions at the bubble surface are satisfied by forcing a match between the liquid and gas equations.

As a practical matter, we change adaptively the number of Chebyshev modes in the numerical simulation. In the slow expansion and most of the collapse, only about six Chebyshev modes are necessary. As the bubble collapses and the temperatures and velocities increase, more modes are needed. We follow Kamath & Prosperetti (1989) and monitor the ratio of the first and last Chebyshev coefficient of all the fields. If the maximum ratio is greater than 10^{-5} we add two more Chebyshev modes. If the ratio is less than 10^{-7} we remove two Chebyshev modes. If these prescriptions are made more conservative, there is little effect on the computations other than increasing the computation time. During the main collapse, a maximum of 16 to 20 modes is typically necessary. Due to the small number of modes we use matrix-vector multiplication to evaluate spatial derivatives rather than making use of the fast transform and recursion relations.

Although the typical runs involve a fairly small number of modes, we emphasize that the numerical algorithm is capable of tracking the evolution of a strong shock, if one occurs. A shock can be artificially promoted, for example, in the computation of

a pure argon bubble where $P_a = 1.3$ and $R_0 = 4.5\,\mu$m but the ratio of specific heats is set artificially low at $\gamma = 1.2$. Such a low value of γ leads to diminished compression heating of the bubble contents; this promotes shock formation by the mechanism discussed in Vuong *et al.* (1999).

We march the equations forward in time with a second-order-accurate predictor-corrector method. The time step is adaptively controlled by monitoring the diffusion coefficients, bubble radius, and velocities. In linear advection and diffusion equations, stability is governed by $c\Delta t/\Delta x$ and $v\Delta t/\Delta x^2$ respectively (c and v are a wave speed and diffusion coefficient). While it is not feasible to determine stability criteria for nonlinear equations we adjust the time step to hold constant the stability discriminants of the related linear problems. Using scaling arguments it is straightforward to show that the time step should vary with $1/R$, $\hat{\mu}$, $\hat{k}$, and $\hat{D}_{ab}/J$. During the expansion, we reduce the time step to account for the large radius. During the collapse, we reduce the time step to account for increases in the diffusion coefficients due to temperature and pressure increases and the large wave speeds from the rapid bubble motions. The time step is also adjusted whenever we add or remove Chebyshev modes.

The liquid temperature equation is solved in a similar fashion as the gas dynamic equations. In order to handle the semi-infinite domain, the liquid temperature is approximated with rational Chebyshev polynomials (Boyd 1987). Explicitly, this approximation is

$$\theta(s,t) \approx \sum_{n=0}^{M} c_n(t) T L_n(s), \qquad (2.15)$$

where $c_n(t)$ are the time-dependent rational Chebyshev coefficients, and $TL_n(s)$ are the rational Chebyshev polynomials. The collocation points in the liquid are located at

$$s_k = L \cot^2 \left[\frac{\pi(2k+1)}{2(2N+2)} \right], \; k = 0, 1, \ldots, N.$$

Rational Chebyshev polynomials are related to Chebyshev polynomials by the following relation:

$$TL_n(y) \equiv T_n(x),$$

where the relation between x and y is

$$y \equiv L(1+x)/(1-x)$$

and L is the map parameter. For the diffusion equation, choosing the map parameter to be equal to the penetration depth works well. For our problem the map parameter is 0.1.

The liquid temperature equation is marched forward with a first-order implicit method. An implicit method is necessary because the fine spacing of the points near the bubble wall places draconian restrictions on time steps for explicit methods. A first-order method is used because the liquid equation is written in nonlinear time, and therefore the integration time step constantly changes.

As with the gas dynamic equations, the number of modes is adaptively changed throughout the calculation. Again, approximately six modes is adequate through the slow bubble motions, and 20 modes is adequate at the time of collapse.

Many standard tests were undertaken for stability and convergence; we increased and decreased the resolution in both time and space. We tried various criteria for adding and removing Chebyshev modes. We checked the mass transfer equations by ensuring the results were not dependent on which species was labelled A or B. We
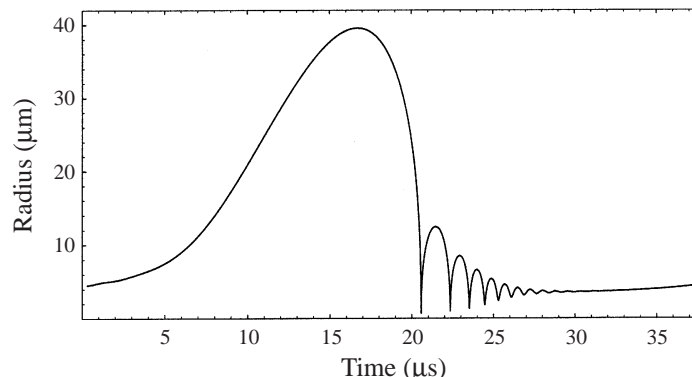
FIGURE 1. Radial response of the bubble to one cycle of the applied acoustic field. The bubble is He–Ar (10% mass He) forced at a pressure amplitude of 1.3.

also monitor global conservation of mass and energy throughout the calculations. These global error estimates are always a fraction of a percent. Finally we also solved the gas dynamics equations with a second-order-accurate finite difference scheme. The spectral method produced nearly identical results much more efficiently.

3. Results

The parameter space for sonoluminescence is quite large. The purpose of the present work is to investigate the phenomenon of species segregation and not to undertake an exhaustive study of the parameter space. The first case we present is a detailed investigation of species segregation in typical single-bubble SL. We then show some trends in single-bubble SL by varying the driving pressure amplitude and the composition of the gas in the bubble. The second case we present has parameters representative of multi-bubble SL. The latter case demonstrates that the species segregation effect is present in multi-bubble and sonochemistry applications as well.

3.1. *Single-bubble sonoluminescence*

We begin by investigating a representative single-bubble SL case with the following parameters: $P_{l,o} = 101$ kPa, $R_0 = 4.5 \, \mu m$, $T_0 = 300$ K, $P_0 = P_{l,o} + 2\sigma_0/R_0$, $P_A = 1.3$, and $\omega/2\pi = 26.5$ KHz. The bubble contains a helium–argon mixture composed of 10% helium by mass (52.58% helium on a mole basis). The radial response of this bubble to one cycle of the applied acoustic field is shown in figure 1. Hereafter, we shall focus on the first main collapse of the bubble which occurs at approximately 20.6 μs from the beginning of the cycle. In figure 2 we show the evolving radial position of selected marker particles in the bubble interior on two time scales which differ by two orders of magnitude. Time is shifted in this figure to put zero at the point of minimum radius; the marker particles were evenly spaced in the reference configuration. On the 100 ns time scale the collapse is quite sharp but on the 1 ns time scale, the bubble smoothly reaches the minimum radius and expands.

In figure 3 we show the temperature history of the bubble centre on the same two time scales as figure 2. The temperature rises an order of magnitude on a 1 ns time scale to a maximum of approximately 42 000 K. Figures 2 and 3 are demonstrations that the bubble motion at minimum radius and the temperature peak occur on a time scale of several hundred pico-seconds. On the 100 ns scale both the dynamic and thermal response of the bubble appear nearly singular.
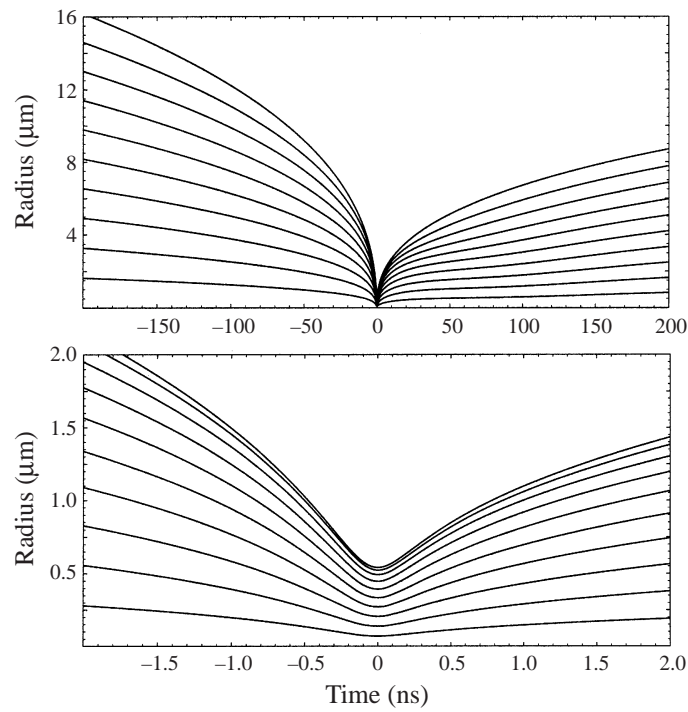
FIGURE 2. Radial response of the bubble to the applied acoustic field at the main collapse on two time scales. The marker particles were evenly spaced in the reference configuration. The outermost marker particle shows the evolving position of the interface. The bubble is He–Ar (10% mass He) forced at a pressure amplitude of 1.3.
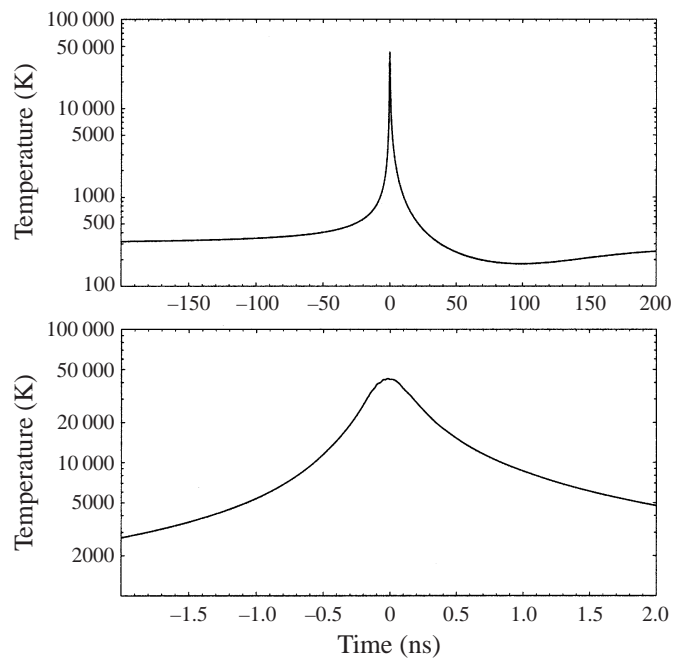

FIGURE 3. Temperature of the centre of the bubble as a function of time at the main collapse. The bubble is He–Ar (10% mass He) forced with a pressure amplitude of 1.3.
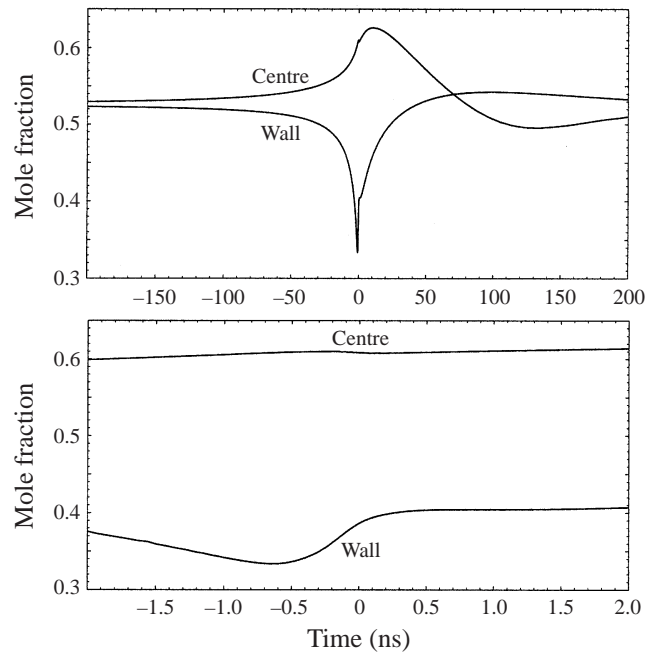
FIGURE 4. Composition history of marker particles at the centre and at the bubble wall as a function of time. The wall particle reaches the lowest mole fraction of helium while the centre reaches the maximum. The bubble is He–Ar (10% mass He) forced with a pressure amplitude of 1.3.

In figure 4 we show the helium mole fraction at the bubble wall and centre of the bubble as a function of time. The same two time scales from the previous two figures are used here. Close examination reveals that compositional inhomogeneities develop much more slowly than the peak dynamic and thermal fields. Over the time scale of the peak dynamic and thermal response the composition field in the bubble is nearly a material field. The species segregation is driven by the slow build up and release of heat throughout the collapse and not by the short burst of energy supplied to the bubble contents at the point of minimum radius. One observes that the mole fraction of helium at the bubble wall decreases to a minimum slightly before $t = 0$ then increases. In contrast, helium continues to accumulate at the centre for some time after the collapse and then eventually the centre becomes slightly argon rich during the expansion. We note that at the extreme moment of the collapse ($t = 0$) the helium fraction monotonically decreases from the centre to the wall.

An alternative view of the composition field is provided in figure 5. In this figure we show snapshots of the composition field within the bubble at intervals of 2 ns with the gray scale indicating the mole fraction of helium. Black indicates argon rich and white indicates helium rich. Upon close inspection we see that the argon is heavily concentrated in a thin region near the wall up to the time of minimum radius. As the bubble expands, the helium continues to move to the centre while the sharp argon 'shell' relaxes by diffusion. We remark that at the main collapse, the mole fraction of the argon-rich outer shell of gas would be slightly different as a consequence of gas transfer into the water. A mass transfer calculation we performed shows this to be a small effect, however. Mass flux of inert gas into the liquid is therefore neglected in the present work.

A careful examination of the terms in the diffusive mass flux shows which gradients drive the species segregation. Before the final stages of the main collapse a negative
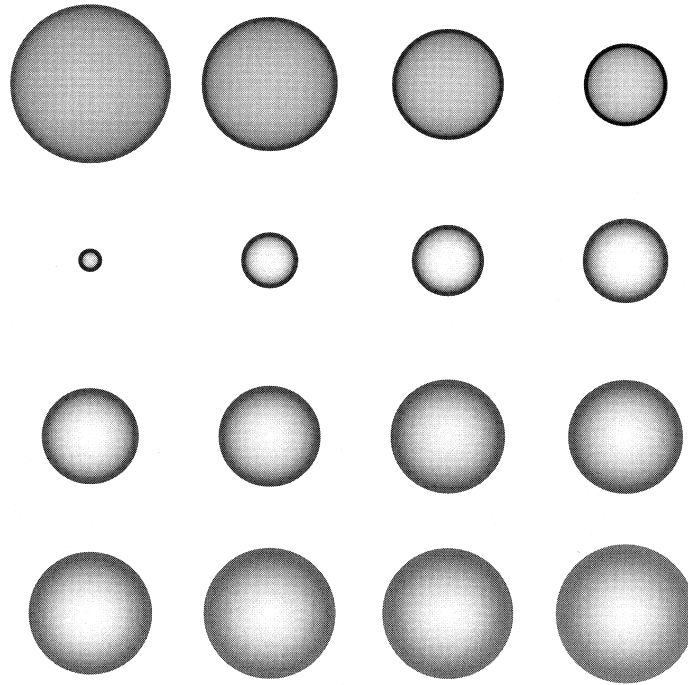
FIGURE 5. Composition field and radius of the bubble around the time of minimum radius. The gray scale is set so that pure black is the minimum in mole fraction of helium that occurred in this case and pure white is the maximum. A uniformly gray disk would indicate uniform composition. The frames are 2 ns apart from −8 to 24 ns from left to right, then down. The bubble is He–Ar (10% mass He) forced with a pressure amplitude of 1.3.

temperature gradient and a positive pressure gradient grow in the bubble. The centre heats by compression, while the bubble wall remains relatively cool due to rapid heat transfer out of the bubble. Also, as the wall accelerates to the minimum radius a compression wave develops at the wall. Both forces act in the same direction and concentrate the helium at the centre. For this particular gas mixture and pressure amplitude, the thermal diffusion causes about 80% of the species segregation up to this point in time.

As the bubble approaches its minimum radius, the bubble wall decelerates and the compression wave proceeds towards the centre. As the compression wave reflects at the centre, the pressure diffusion vector changes sign and there is a strong tendency for the helium to leave the centre of the bubble. The thermal diffusion still drives the helium toward the centre. While the pressure diffusion term is dominant over the thermal diffusion when the compression wave reflects at the origin, the helium remains in the centre because the pressure diffusion term is too short-lived to be of much consequence.

Upon expansion of the bubble after the collapse, the compression wave dies very quickly. The temperature field begins to relax on the same time scale that it was created. The negative temperature gradient that persists after the collapse continues to concentrate the helium in the centre for some time. As the bubble expands, the contents cool and the helium begins to leave the centre. Later in time the rapid expansion causes the temperature at the centre to become lower than the initial temperature (about $\hat{T} = 0.6$) and the bubble wall returns to the far-field liquid temperature. The

temperature gradient in the bubble thus changes sign and thermal diffusion drives the helium to the relatively warm wall. As the bubble reaches the next radius maximum, the bubble returns to essentially uniform temperature and species composition.

The development of the concentration field may be clarified through scaling arguments. From the mass transport equation, it is straightforward to show the time scale for mass diffusion (in dimensional terms) varies as $R^2/D_{ab}(T)$. From kinetic theory, we know $D_{ab} \propto T^{3/2}/p$; hence $\rho D_{ab} \propto T^{1/2}$, or $D_{ab} \propto R^3 T^{1/2}$. Thus, the diffusion time scale is proportional to $1/(RT^{1/2})$. When R is small and T is large at the collapse, the product $RT^{1/2}$ has a value not much different from its value at ambient conditions ($0.5 \, \mu s$). In the early part of the collapse, the time scale for bubble motions (i.e. $R/\dot{R}(t)$) is of the same order as the mass diffusion time scale. The relatively slow build up of temperature and pressure gradients prior to the main collapse therefore has significant time to drive the diffusive mass flux. The peak thermal and pressure response occurs on a much more rapid time scale. As the bubble reaches minimum radius, the time for the compression wave to reflect at the bubble centre is approximately $100 \, ps$. The compression wave acts very briefly and only creates a small wiggle in the composition fields (visible in figure 4).

The peak in thermal diffusion also occurs on a very rapid time scale compared to the time scale for mass transfer. Thus, the composition field does not have time to react to the most extreme temperature gradients. It is worth emphasizing that the thermal diffusion term is proportional to the relative temperature gradient. Therefore, the absolute temperature is not the important quantity, but rather the ratio T_{centre}/T_{wall}. One should note that while the time scale of the *peak* in the relative temperature gradient is very rapid, a significant relative gradient exists for a much longer time.

In the interest of comparison, we study the same bubble but with the diffusive mass flux disallowed. It is interesting to note that the peak temperature of the segregating case is virtually identical to the non-segregating case. The total energy at the centre (internal energy) is higher in the segregating case because the diffusive mass flux carries the higher enthalpy helium into the centre. Helium has a higher enthalpy than argon (based on mass) as a consequence of its lower molecular mass. The specific heat in the segregating case is also higher in the centre due to the increase in helium concentration at the centre. These two effects compensate one another such that the temperature is fairly insensitive to whether or not diffusive mass flux is included. We note no discernible difference in the overall bubble dynamics between the two cases.

Upon comparison, the segregating and non-segregating bubble wall temperatures are very similar as well. This is peculiar at first glance because the thermal conductivity near the wall is quite different in the two cases. In the segregating case the thermal conductivity at the wall is (briefly) lower because this zone is argon rich. Argon has a much lower thermal conductivity than helium due to the large difference in molecular mass. This has little effect on the wall temperature for all the cases we investigated. It appears that the bubble dynamics drives the diffusive mass transfer, but the resulting species segregation has little effect on the bubble dynamics and temperature field. We note that these observations hold true for all the cases that we examined with noble gases. It is unknown whether this observation will apply to diatomic or polyatomic species.

As a final note on this particular case, the EOS includes a computation of the degree of ionization. For the most extreme conditions we encounter, the gas has approximately 10^{-4} free electrons per atom. Therefore, neglecting ionization is consistent with our computation of the transport properties.

Different pressure amplitudes show similar qualitative behaviour with quantitative differences in the peak temperatures and amount of species segregation. We computed

the same helium–argon bubble forced at pressure amplitudes of 1.1 and 1.2. Lower pressure amplitudes result in lower temperature and pressure gradients and therefore less species segregation. Also, the percentage of species segregation attributable to pressure diffusion increases with pressure amplitude.

Mixtures of different noble gases behave similarly. We computed bubbles composed of xenon–helium and argon–xenon at pressure amplitudes of 1.1, 1.2, and 1.3. The amount of species segregation at a given forcing amplitude depends on the thermal diffusion factor and the difference between the mole and mass fractions (i.e. molecular weight difference). At pressure amplitudes of 1.1 the helium–argon bubble has about 10% more maximum species segregation than the helium–xenon bubble. This difference is due to the larger relative temperature gradient and larger thermal diffusion factor (for the mole fractions we selected) in the helium–argon bubble. At pressure amplitudes of 1.3 the xenon–helium bubble has approximately 15% more segregation than the helium–argon bubble. At this pressure amplitude, the pressure gradient is similar between the two gas mixtures; however, the pressure diffusion term is larger in the helium–xenon case because of the larger difference in molecular weight of the species. The thermal conductivity of the gas is also important since the relative temperature gradient between the bubble wall and the centre drives species segregation. The qualitative behaviour of the composition field is very similar for these other mixtures, with differences in the amount of species segregation and the relative role of pressure and temperature diffusion.

3.2. *Multi-bubble sonoluminescence*

Finally, we consider a case representative of multi-bubble SL. We use the experimental inference of bubble radius and pressure amplitude from Gaitan *et al.* (1992) to make the connection between single- and multi-bubble SL. The case we investigate has the same parameters as the single-bubble case we examined in detail except that $R_0 = 17.5\,\mu$m. We note that such a bubble, driven at the elevated amplitudes we consider below, is known to be shape unstable (see Holt & Gaitan 1996 and Hilgenfeldt, Lohse & Brenner 1996). Nevertheless a spherical calculation is instructive because it demonstrates that the species segregation occurs even over the length scales of these much larger bubbles.

The maximum temperature at the bubble centre for the multi-bubble case is 22 000 K which occurs when the bubble radius is near its minimum of 3.2 μm. The maximum difference in helium mole fraction between the wall and centre is 0.23 and occurs 4 ns before the time of minimum radius. This should be compared to figure 4 where the maximum of 0.27 occurred about 0.6 ns before the time of minimum radius. The pressure diffusion is less important in this example than the single-bubble case, owing to the milder collapse.

The amount of species segregation in the multi-bubble case is still significant even though the bubble collapse is milder than the single bubble. While the peak temperature is lower than the single-bubble case, the ratio T_{centre}/T_{wall} is higher in the multi-bubble example. The relative temperature gradient is larger due to the increase in the liquid Péclet number with initial bubble radius. The bubble wall reaches a maximum of 1200 K in the multi-bubble example as opposed to 4600 K in the single-bubble example. We see that the maximum temperature of the centre is about twice as large for the single-bubble example but the wall temperature is almost four times greater. We also see that the ratio of the mass diffusion time scale to bubble motion time scale is somewhat lower in the multi-bubble case around the time of collapse. Thus, the thermal diffusion is stronger and has more time to act

in the multi-bubble case. The compression wave proceeding the collapse is much milder in the multi-bubble case than in the single bubble, resulting in lower pressure diffusion in the multi-bubble case. Therefore, with the larger bubble we still get very significant thermal diffusion (more so than the single-bubble case) but very little pressure diffusion.

3.3. *Mass exchange equilibrium with the liquid*

One potential consequence of species segregation is that the mole fraction of a dissolved gas mixture in the liquid may not equal the mole fraction of the gas inside the bubble. Because some species are at higher concentrations at the wall during part of the cycle, these components could be preferentially absorbed in the liquid. To address this issue we make use of the well-known threshold condition for rectified diffusion (Eller & Flynn 1965; see also Fyrillas & Szeri 1994 and Vuong, Fyrillas & Szeri 1998):

$$\frac{C_{A,\infty}}{C_{A,s,ref}} = \frac{\int_0^T R^4(\tau)P_A(\tau)\mathrm{d}\tau}{\int_0^T R^4(\tau)\mathrm{d}\tau}. \tag{3.1}$$

Here $C_{A,\infty}$ is the far-field concentration of species A, $C_{A,s,ref} = P_{ref}/k(T)$, $k(T)$ is Henry's constant, and P_A is the partial pressure of species A at the bubble wall.

In order to determine whether the species segregation affects the mass exchange equilibrium between the bubble and the liquid, we compare the results of this equation for a segregating and non-segregating mixture. For an ideal mixture the partial pressure of one species is given by $P_A = x_A P$. For a non-segregating mixture, x_A is constant and may be pulled out of the integral. We compare the threshold integral using the time-varying mole fraction of the segregated species at the wall with that obtained with x_A constant. A difference in these integrals indicates that species segregation affects the bubble equilibrium.

For the cases discussed in this paper, there is no difference when we compute the integral using the variable mole fraction or the constant initial mole fraction. Even though the species do segregate significantly, the time spent separated is relatively short compared to the time of the entire cycle. Also, the separation occurs when the radius is smallest and thus when the radius is taken to the fourth power, this part of the cycle contributes less to the total integral.

These results indicate that the relationship between mole fraction of the dissolved species and the mole fraction of the gas in the bubble can be determined without taking into account species segregation. This does not mean that the mole fraction of the dissolved gas is equal to the mole fraction of the gas in the bubble; these can be very different. When determining the mole fraction of the gas in the bubble, one must take into account the difference in DC_∞/M (Lohse & Hilgenfeldt 1997), but the assumption of a uniform mixture for these calculations appears to be a good approximation. Species segregation may play a role for the absorption of species that are short lived due to chemical reactions. The species may only exist for a brief time and never be exposed to the bubble wall.

4. Conclusions

We made use of the tools of computational fluid dynamics to study the consequences of diffusive mass flux in a sonoluminescence bubble containing a monatomic gas

mixture. Principally by the mechanism of thermal diffusion, i.e. diffusion driven by a temperature gradient, the species in a gas mixture partially segregate over a time scale much longer than the time scale of the temperature peak at the bubble centre. Mass diffusion driven by a pressure gradient, while numerically dominant for a short time, is too short-lived to have much impact on the composition field of the bubble interior. The temperature gradient responsible for most of the species segregation develops as a consequence of both compression heating of the bubble contents and heat flux to the surrounding liquid during the early and middle stages of the main collapse.

The species segregation takes the form of a higher fraction of the light species near the bubble centre at the main collapse, whereas the cooler region near the bubble wall is richer in the heavier species. The extent of species segregation increases with the amplitude of the acoustic drive, and with dissimilarity of the species present in the mixture. We note that with more complex molecules, the sign of the thermal diffusion coefficient depends on both the size and the weight of the molecule.

Because the light species migrates to the centre at the main collapse, there is a greater concentration of internal energy at the bubble centre when the diffusive mass flux is taken into account, rather than neglected. However, the temperature field is not significantly different in either case. Similarly, species segregation has little effect on the mass exchange equilibrium between the bubble and the surrounding liquid.

In summary, we have shown that there is significant species separation in sonoluminescence bubbles. This will likely play a role in further explanation of the light emission mechanism (Moss *et al.* 1999), and will certainly be important to the chemistry and applications of sonoluminescence.

Appendix. Transport properties

The equations for the transport properties are taken from the Chapman–Enskog theory with corrections for high temperature and pressure. Those we used are taken from Reid, Prausnitz & Poling (1987), Hirschfelder, Curtiss & Bird (1954) and Chapman & Cowling (1990).

A.1. *Transport properties of the mixture*

The viscosity and thermal conductivity of a single-component gas are

$$\mu \times 10^7 = 266.93 \frac{\sqrt{MT}}{\sigma^2 \Omega^{2,2}(T^*)}, \tag{A1}$$

$$k = \frac{15}{4} \frac{\bar{R}}{M} \mu, \tag{A2}$$

where M is the molecular weight, T is the temperature in Kelvin, σ is the collision diameter in Angstroms, $\Omega^{2,2}(T^*)$ is the collision integral using the Lennard–Jones 12-6 as tabulated in the Appendix (Table I-M) of Hirschfelder *et al.* (1954), T^* is the reduced temperature Tk/ϵ, and ϵ/k is the potential parameter in Kelvin. The viscosity, μ, is given in $g\,cm^{-1}\,s$ and thermal conductivity, k, in $cal\,cm^{-1}\,s\,K$.

Rather than using the lengthy mixture equations for viscosity and thermal conductivity, we use the mixing rules of Chung (see Equations 9-5.24 to 9-5.40 in Reid *et al.* 1987) to get mean effective molecular parameters for the single-component equations. The mean values (denoted by the subscript *m*) are used in the single-component equations to give properties for the mixture. The equations are

$$\sigma_{ij} = (\sigma_i \sigma_j)^{1/2}, \tag{A 3}$$

$$\frac{\epsilon_{ij}}{k} = \left(\frac{\epsilon_i}{k} \frac{\epsilon_j}{k} \right)^{1/2}, \tag{A 4}$$

$$M_{ij} = \frac{2 M_i M_j}{M_i + M_j}, \tag{A 5}$$

$$\sigma_m^3 = \sum_i \sum_j x_i x_j \sigma_{ij}^3, \tag{A 6}$$

$$\frac{\epsilon_m}{k} = \frac{\sum_i \sum_j x_i x_j (\epsilon_{ij}/k) \sigma_{ij}^3}{\sigma_m^3}, \tag{A 7}$$

$$T_m^* = T k / \epsilon_m, \tag{A 8}$$

$$M_m = \frac{\sum_i \sum_j x_i x_j (\epsilon_{ij}/k) \sigma_{ij}^2 M_{ij}^{1/2}}{(\epsilon_m/k) \sigma_m^2}, \tag{A 9}$$

where x_i is the mole fraction of the *i*th species. This mixing rule is accurate to within 5% for ordinary conditions, although it has not been tested at the extreme temperatures and pressures encountered in SL.

The binary diffusion coefficient for a low-density gas is given as

$$D_{12} = 0.0026280 \frac{\sqrt{T^3/M_{12}}}{p \sigma_{12}^2 \Omega_{12}^{1,1}(T_{12}^*)}, \tag{A 10}$$

where p is the pressure in atmospheres and D_{12} is given in $\mathrm{cm^2\,s^{-1}}$. The equations for the low-density viscosity, thermal conductivity, and binary diffusion coefficients from the Chapman–Enskog theory are well known and are quite accurate for monatomic gases at reasonable temperatures using a Lennard–Jones 12-6 potential (Hirschfelder *et al.* 1954; Chapman & Cowling 1990).

A.2. *Correction for high densities*

To correct for high density we use Enskog's correction for a dense gas of rigid spheres. These equations are derived for a single-component fluid, but we simply assume that the gas mixture behaves as a single-component fluid with the mean effective parameters. This is a very crude correction but it does predict the proper trends in the properties as the density increases. The equations are

$$\mu/\mu_0 = b_0 \bar{\rho}(1/y + 0.8 + 0.761y), \tag{A 11}$$
$$k/k_0 = b_0 \bar{\rho}(1/y + 1.2 + 0.755y), \tag{A 12}$$
$$y = \frac{p}{\rho \bar{R} T} - 1, \tag{A 13}$$

where the subscript 0 means the low-pressure value (as computed from above), $\bar{\rho}$ is the molar density, and b_0 is the excluded volume $2/3\pi N\sigma^3$, where N is Avogadro's number. We compute y, the compressibility minus one, with the following approximation:

$$y = (b_0\bar{\rho}) + 0.6250(b_0\bar{\rho})^2 + 0.2869(b_0\bar{\rho})^3 + 0.115(b_0\bar{\rho})^4. \qquad (A\,14)$$

The binary diffusion coefficient for a mixture is given from the dense gas theory by

$$D_{12}/D_{12}^0 = 1/Y_{12}, \qquad (A\,15)$$

$$Y_{12} = 1 + \tfrac{2}{3}\,n_1\sigma_1^3 \left(\frac{\sigma_1 + 4\sigma_2}{4\sigma_1 + 4\sigma_2}\right) + \tfrac{2}{3}\,n_2\sigma_2^3 \left(\frac{\sigma_2 + 4\sigma_1}{4\sigma_1 + 4\sigma_2}\right), \qquad (A\,16)$$

where $n_{1(2)}$ are the number densities. The method we use provides results very close to those obtained with the full dense gas mixture theory but our method is more computationally efficient.

A.3. *Correction for high temperatures*

To account for high temperature we use a temperature-dependent collision diameter as computed from the equation of state. This correction simulates the effect of temperature on atomic collisions by allowing the molecules to come into closer contact upon collision. We use the equation of state to extract a temperature-dependent sphere diameter in the following way. We set the thermal kinetic energy equal to the $T = 0$ energy from the EOS (i.e. $kT = E\,(T = 0, \rho)$) to determine the density at close packing for a particular temperature. We relate this density to a sphere diameter assuming tightly packed spherical molecules. This temperature-dependent sphere diameter is then used in the Chapman–Enskog equations. The collision diameter data were fitted with the following equations, in the temperature range 200–200 000 K:

$$\sigma_{Ar} = -5412.661 + 3.103/T - 627.974/T^{0.01} + 6043.671/T^{0.001}, \qquad (A\,17)$$

$$\sigma_{He} = -513.494 - 4.187/T - 30.767/T^{0.01} + 548.282/T^{0.001}, \qquad (A\,18)$$

$$\sigma_{Xe} = -6181.519 + 5.999/T - 720.213/T^{0.01} + 6905.133/T^{0.001}, \qquad (A\,19)$$

where σ_i is in Angstroms.

The equation for thermal diffusion is not included here because it is quite lengthy. We used the high-pressure thermal diffusion equation for a binary gas mixture (see Section 16.9 in the 2nd edition of Chapman & Cowling). It should be noted that the low-pressure thermal diffusion equation (for example, Equation 8.2-50 in Hirschfelder *et al.* 1954), gives very similar results.

REFERENCES

AMDUR, I. & MASON, E. A. 1954 Properties of gases at very high temperatures. *Phys. Fluids* **1**, 370–383.

BERNSTEIN, L. S., ZAKIN, M. R., FLINT, E. B. & SUSLICK, K. S. 1996 Cavitation thermometry using molecular and continuum sonoluminescence. *J. Phys. Chem.* **100**, 6612–6619.

BIRD, R. B., STEWART, W. E. & LIGHTFOOT, E. N. 1960 *Transport Phenomena*. J. Wiley and Sons.

BOYD, J. P. 1987 Orthogonal rational functions on a semi-infinite interval. *J. Comput. Phys.* **70**, 62–88.

BOYD, J. P. 1989 *Chebyshev and Fourier Spectral Methods*. Springer.

CANUTO, C., HUSSAINI, M. Y., QUARTERONI, A. & ZANG, T. A. 1988 *Spectral Methods in Fluid Dynamics*. Springer.

CAREY, V. P. 1992 *Liquid-Vapor Phase Change Phenomena*. Taylor and Francis.

CHAPMAN, S. & COWLING, T. G. 1990 *The Mathematical Theory of Non-Uniform Gases.* Cambridge University Press.

ELLER, A. & FLYNN, H. G. 1965 Rectified diffusion during nonlinear pulsations of cavitation bubbles. *J. Acoust. Soc. Am.* **37**, 493–503.

FYRILLAS, M. M. & SZERI, A. J. 1994 Dissolution or growth of soluble, spherical, oscillating bubbles. *J. Fluid Mech.* **277**, 381–407.

GAITAN, D. F., CRUM, L. A., CHURCH, C. & ROY, R. A. 1992 Sonoluminescence and bubble dynamics for a single, stable, cavitation bubble. *J. Acoust. Soc. Am.* **91**, 3166–3183.

HILGENFELDT, S., LOHSE, D. & BRENNER, M. P. 1996 Phase diagrams for sonoluminescing bubbles. *Phys. Fluids* **8**, 2808–2826.

HIRSCHFELDER, J. O., CURTISS, C. F. & BIRD, R. B. 1954 *Molecular Theory of Gases and Liquids.* J. Wiley and Sons.

HOLT, R. G. & GAITAN, D. F. 1996 Observation of stability boundaries in the parameter space of single bubble sonoluminescence. *Phys. Rev. Lett.* **77**, 3791–3794.

KAMATH, V. & PROSPERETTI, A. 1989 Numerical integration methods in gas-bubble dynamics. *J. Acoust. Soc. Am.* **85**, 1538–1548.

LOHSE, D., BRENNER, M. P., DUPONT, T. F., HILGENFELDT, S. & JOHNSTON, B. 1997 Sonoluminescencing air bubbles rectify argon. *Phys. Rev. Lett.* **78**, 1359–1362.

LOHSE, D. & HILGENFELDT, S. 1997 Inert gas accumulation in sonoluminescing bubbles. *J. Phys. Chem.* **107**, 6986–6997.

MOSS, W. C., YOUNG, D. A., HARTE, J. A., LEVATIN, J. L., ROZSNYAI, B. F., ZIMMERMAN, G. B. & ZIMMERMAN, I. H. 1999 Computed optical emissions from a sonoluminescing bubble. *Phys. Rev. E* **59**, 2986–2992.

PROSPERETTI, A. & LEZZI, A. 1986 Bubble dynamics in a compressible liquid. Part 1. First-order theory. *J. Fluid Mech.* **168**, 457–477.

REID, R. C., PRAUSNITZ, J. M. & POLING, B. E. 1987 *Properties of Gases and Liquids.* McGraw Hill.

SENGERS, J. V. 1965 Thermal conductivity and viscosity of simple fluids. *Intl J. Heat Mass Transfer* **8**, 1103–1115.

VUONG, V. Q., FYRILLAS, M. M. & SZERI, A. J. 1998 The influence of liquid temperature on the sonoluminescence hot spot. *J. Acoust. Soc. Am.* **104**, 2073–2076.

VUONG, V. Q. & SZERI, A. J. 1996 Sonoluminescence and diffusive transport. *Phys. Fluids* **8**, 2354–2364.

VUONG, V. Q., SZERI, A. J. & YOUNG, D. A. 1999 Shock formation within sonoluminescence bubbles. *Phys. Fluids* **11**, 10–17.

YUAN, L., CHENG, H. Y., CHU, M. C. & LEUNG, P. T. 1998 Physical parameters affecting sonoluminescence: A self-consistent hydrodynamic study. *Phys. Rev. E* **57**, 4265–4280.